Journal of Marine Research, 63, 705–728, 2005

Thermohaline circulation induced by bottom friction in sloping-boundary basins

by Johan Nilsson[1,2], Gösta Walin[3] and Göran Broström[1]

ABSTRACT

We show that a velocity field in geostrophic and hydrostatic balance on the *f*-plane can be diagnosed from an arbitrarily prescribed distribution of buoyancy in a basin with closed depth contours. We emphasize the steady-state circulation associated with a large-scale horizontal buoyancy gradient, attained in the absence of wind forcing. For inviscid motion, the diagnosed field contains a free barotropic along-isobath flow which can be chosen arbitrarily, e.g. in such a way that the buoyant "southern" pool of surface water essentially recirculates. Including bottom friction, we show that steady motion requires that the net Ekman transport across closed depth contours must vanish. This constraint determines the free barotropic motion and thereby the entire velocity field, which proves to be independent of the strength of the bottom friction. The barotropic flow component serves to create a "thermohaline" circulation, i.e. a circulation which tends to spread the buoyant water horizontally. Analytical solutions and results from a numerical experiment are presented to illustrate the steady flow resulting in a basin where the upper-ocean density increases across the basin.

1. Introduction

The present paper investigates the steady linear *f*-plane circulation that is attained in a basin with closed depth contours in the absence of wind forcing. The focus is on the geophysically relevant case where the upper-ocean buoyancy decreases "northward" in the basin, as outlined in Figure 1. The aim is to determine the velocity field from the buoyancy distribution. Thus, we are essentially revisiting a classical problem in dynamical oceanography (see Park and Guernier, 2001, for a brief overview). As in the classical approach, we assume that the velocity field at the leading order obeys the hydrostatic and geostrophic balance. This assumption yields the thermal wind balance, which specifies the velocity field relative to an unknown barotropic flow component.

The presence of closed depth contours has an important dynamical consequence: Any barotropic pressure distribution which is a function of the basin depth alone represents an unforced steady flow in geostrophic balance. Such depth-independent isobath-following

1. Department of Meteorology, Stockholm University, SE-10691 Stockholm, Sweden.
2. Corresponding author. ***email: nilsson@misu.su.se***
3. Department of Oceanography, Earth Sciences Centre, Göteborg University, Box 460, SE-40530 Göteborg, Sweden.

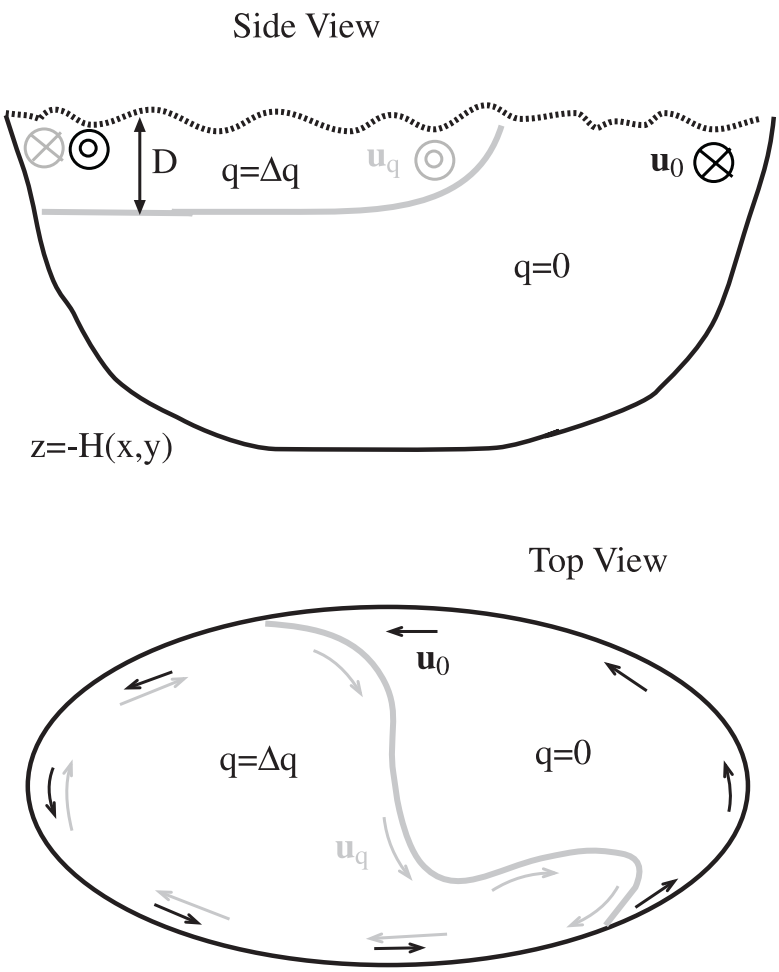

Figure 1. Illustration of a steady two-layer flow in a basin with closed depth contours, analyzed in Section 3b. The flow is composed of two components: $\mathbf{u}_q$ related to the buoyancy field q and $\mathbf{u}_0$, an isobath-following barotropic flow which is unconstrained in the inviscid limit. In the presence of friction, $\mathbf{u}_0$ is determined by the constraint that the bottom Ekman transport must integrate to zero around the isobaths. Note that since $\mathbf{u}_q \cdot \nabla D = 0$, only $\mathbf{u}_0$ acts to redistribute the buoyant surface layer.

flows are collectively known as the geostrophic mode (cf. Greenspan, 1968, Section 2.6). In the inviscid limit, there is no restriction on the geostrophic mode, which accordingly can be specified arbitrarily. However, we demonstrate that viscosity, no matter how small, constrains the free barotropic flow. In the presence of weak viscosity, we show that the geostrophic mode is determined by the requirement that the cross-isobath transport in the bottom Ekman layer integrates to zero in a steady state.

In the context of steady homogeneous flow, it is well established that the total Ekman

transport must integrate to zero around a closed depth contour (cf. Greenspan, 1968, Section 2.17). If the wind drives surface Ekman transport across a closed depth contour, an isobath-following geostrophic flow will arise that induces a compensating transport in the bottom Ekman layer. Thus, given the boundary-layer physics and the wind forcing, the steady-state velocity on closed depth contours (or more generally H/f contours) can be calculated. This procedure was first used by Kamenkovich (1963) in an investigation of the Antarctic Circumpolar Current. Subsequently, similar ideas have been used in oceanographic studies by Walin (1972), Nøst and Isachsen (2003), and Isachsen *et al.* (2003). It should be noted that in the case of homogeneous flow, the presence of friction implies that a state of no motion is attained if the wind forcing is switched off.

The present novel result, pertaining to a stratified flow, is that bottom buoyancy variations in the presence of friction give rise to an isobath-following barotropic flow, even in the absence of wind forcing. We show that given the boundary-layer physics and the buoyancy distribution, the barotropic velocity on closed isobaths can be determined, hereby providing the absolute geostrophic velocity field. The resulting flow depends on the presence of friction but not on its strength.

In essence, we derive a dynamical constraint from viscous Ekman-layer physics, which on closed isobaths determines the geostrophic flow associated with a given buoyancy field. Accordingly, we impose no constraints on the advection of buoyancy nor on the mixing necessary for maintaining the buoyancy field in a steady state. We note, however, that constraints on the advection of buoyancy have been employed in studies on the relation between the hydrographic distribution and the large-scale ocean circulation. In the theory of the ideal-fluid thermocline, pioneered by Welander (1959), the advection of buoyancy is taken to be zero outside the surface Ekman layer. Marshall (1995), who studied the dynamics of an ideal-fluid thermocline in the presence of bottom topography, presumed that the advection of bottom density is zero. Also observationally-based studies generally impose constraints on the mixing to estimate the absolute geostrophic velocity. For instance, Bogden *et al.* (1993), in a study of the North Atlantic circulation, adjusted a barotropic flow along open H/f-contours in order to minimize the advection of potential density at mid depths. In a related study, Park and Guernier (2001) followed the idea of Marshall (1995) and assumed that the advection of bottom density is zero.

In the present study, however, the isobath-following barotropic flow generally advects the bottom density, as delineated in Figure 1. In fact, we find that along-isobath variations of bottom buoyancy give rise to an advection of the buoyancy field. In this respect, the present study has similarities with the investigations by Chapman and Lentz (1994), Hallberg and Rhines (1996), and Lentz and Helfrich (2002), which deal with various aspects of time-dependent motion in a rotating fluid where the buoyancy varies along the depth contours. Further, we note that Spall (2004, 2005) and Walin *et al.* (2004) employed numerical and analytical methods to study aspects of the time-mean circulation in f-plane basins with sloping boundaries. In particular, Walin *et al.* (2004) analyzed and discussed the role of barotropic currents for transporting buoyant water masses along closed isobaths.

The present work may be viewed as an extension of their study by providing a theory for how the strength of the isobath-following barotropic flow is controlled. It should be noted that the study by Spall (2005, this issue), focusing on a basin with open isobaths, represents an interesting complement to the present study of the dynamics in basins with closed isobaths.

Evidently the present study, dealing with f-plane flows, has somewhat limited oceanographic applications. We note, however, that f-plane dynamics are of relevance for the circulation in parts of the Nordic Seas and the Mediterranean, where regional closed-isobaths features such as the Lofoten Basin and the southern Adriatic Sea are encountered. Furthermore, the present theoretical considerations apply not only for basins with sloping boundaries but also for regions of closed isobaths around islands and sea mounts. Iceland, where isobaths shallower than 500 m encircle the island, provides an example where the f-plane approximation is relevant. Moreover the present study, besides being interesting in the context of geophysical fluid dynamics, should provide a step toward a theoretical description of the steady flow within closed H/f-contours on a sphere that arises in presence of spatially varying bottom buoyancy.

We underline that the present study deals with steady geostrophic circulations, i.e. flow fields characterized by small Rossby and Ekman numbers. Thus, we do not address effects of nonlinear dynamics and time-dependent eddies. We note that eddies generally are important for the buoyancy distribution in basins like the Nordic Seas. In particular, eddy fluxes tend to dominate the cross-isobath transport of buoyancy (see e.g. Spall, 2004, 2005). If the eddy-momentum fluxes are sufficiently weak, however, the time-mean velocity and buoyancy fields will be approximately in geostrophic balance. In such situations, the present considerations are expected to provide a leading-order description of the time-mean circulation.

The remainder of the paper is organized as follows. Section 2 presents a theoretical investigation of steady flow in bowl-like basins with horizontal variations of buoyancy. In Section 3, key results are illustrated with analytical results as well as with the outcome of an idealized numerical simulation. In the final section, the limitations and the applicability of the present work is discussed, including some speculations on the role of sloping boundaries for the stability of the thermohaline circulation.

2. Stratified flows in basins with closed depth contours

We consider the linear dynamics of a rotating stratified fluid in the hydrostatic limit on an f-plane. We assume that viscous effects are confined to thin Ekman boundary layers adjacent to the bottom and the free surface. For the interior inviscid part of the flow, the momentum equation is given by

$$\frac{\partial \mathbf{u}}{\partial t} + f\mathbf{k} \times \mathbf{u} = -\rho_r^{-1} \nabla_h p, \tag{1}$$

where $\mathbf{u} = (u, v)$ is the horizontal velocity component, f the Coriolis parameter, $\mathbf{k}$ a vertical unit vector, p the perturbation pressure, and ∇_h the horizontal gradient operator. The hydrostatic equation is given by

$$\frac{\partial p}{\partial z} = -g\rho_r(1 - q), \tag{2}$$

where g is the acceleration of gravity, ρ_r the deep water density, and q the density anomaly.

The continuity equation is given by

$$\frac{\partial u}{\partial x} + \frac{\partial v}{\partial y} + \frac{\partial w}{\partial z} = 0. \tag{3}$$

The vertical velocity obeys the following linearized boundary conditions

$$w(z = 0) = \frac{\partial \eta}{\partial t} + \nabla \cdot \mathbf{m}_w, \; w(z = -H) = -\mathbf{u}_b \cdot \nabla H - \nabla \cdot \mathbf{m}_b, \tag{4}$$

where $\mathbf{u}_b$ is the bottom velocity, η the level of the free surface, and $\mathbf{m}_w$ and $\mathbf{m}_b$ are the boundary layer transports in the top and the bottom Ekman layers, respectively. The properties of the Ekman transport will be dealt with in Section 2b.

By taking the curl of the momentum equation (1) and employing the continuity equation, one obtains

$$\frac{\partial \nabla \times \mathbf{u}}{\partial t} - f\frac{\partial w}{\partial z} = 0. \tag{5}$$

We integrate this equation vertically over the water column, using Eq. (4), to obtain

$$\frac{\partial \eta}{\partial t} - \frac{1}{f}\int_{-H}^{0} \frac{\partial \nabla \times \mathbf{u}}{\partial t}\, dz + \mathbf{u}_b \cdot \nabla H = -\nabla \cdot \mathbf{m}, \tag{6}$$

where $\mathbf{m} = \mathbf{m}_w + \mathbf{m}_b$ is the combined top and bottom Ekman transports.

a. The steady-state interior flow field

From now on, the focus is on time-independent circulation. We integrate the hydrostatic equation upwards from the bottom, which yields

$$p(x, y, z) = g\rho_r \int_{-H}^{z} q\, dz + p_0(x, y) - g\rho_r z. \tag{7}$$

Here, $H(x, y)$ is the basin depth and p_0 is a barotropic pressure anomaly, defined as $p_0(x, y) = p_b(x, y) - g\rho_r H$, where p_b is the bottom pressure. The linearized surface pressure is given by $p(z = 0) = g\rho_r\eta$. Accordingly, Eq. (7) yields the relation

$$\eta(x, y) = \int_{-H}^{0} q dz + p_0/(g\rho_r), \tag{8}$$

where the first term on the right-hand side is known as the steric height anomaly and the second one is the contribution to sea-surface height due to barotropic pressure anomaly p_0.[4]

For time-independent flow, the momentum equation (1) reduces to the geostrophic balance. From (7) we obtain the following expression for the geostrophic velocity

$$\mathbf{u} = \frac{g}{f}\mathbf{k} \times \nabla_h \int_{-H}^{z} q dz + \frac{1}{f\rho_r}\mathbf{k} \times \nabla p_0. \tag{9}$$

By applying Leibnitz's rule of differentiation to the first term on the right-hand side of Eq. (9), we arrive at

$$\mathbf{u} = \frac{g}{f}\mathbf{k} \times \int_{-H}^{z} \nabla_h q dz + \frac{g}{f} q_b \mathbf{k} \times \nabla H + \frac{1}{f\rho_r}\mathbf{k} \times \nabla p_0, \tag{10}$$

where q_b is the density anomaly at $z = -H(x, y)$, i.e.

$$q_b(x, y) = q(x, y, -H). \tag{11}$$

We note that the first term on the right-hand side of (10) represents the thermal-wind velocity relative to zero flow at the bottom. Accordingly, the velocity at the bottom is given by

$$\mathbf{u}_b = \frac{g}{f} q_b \mathbf{k} \times \nabla H + \frac{1}{f\rho_r}\mathbf{k} \times \nabla p_0. \tag{12}$$

Note that the bottom-velocity component associated with q_b is aligned with the depth contours. Obviously the strength of this component varies along the isobaths if q_b does. Note furthermore that p_0 alone accounts for any cross-isobath flow. Finally, it is relevant to mention that $(g/f)q_b|\nabla H|$ can be interpreted as the baroclinic topographic Rossby wave speed (Spall, 2005).

b. The primary along-isobath flow

We will now show that it is possible to determine the bottom velocity in a basin with closed depth contours provided that the buoyancy field $q(x, y, z)$ is known. Accordingly, the buoyancy-related part of the flow field, represented by the first two terms in Eq. (10), is

4. Note that if (8) is used to substitute p_0 in (7), one obtains the more commonly used expression for p that results if the hydrostatic equation is integrated downward from the surface.

taken to be prescribed. The aim is thus to determine the barotropic pressure p_0 and its associated velocity field. Making use of the bottom-velocity relation (12), the steady-state version of Eq. (6) takes the form

$$\mathbf{u}_0 \cdot \nabla H = -\nabla \cdot \mathbf{m}, \tag{13}$$

where

$$\mathbf{u}_0 = \frac{1}{f\rho_r}\mathbf{k} \times \nabla p_0.$$

We use the fact that $\mathbf{u}_0 \cdot \nabla H = \nabla \cdot (H\mathbf{u}_0)$ and integrate Eq. (13) over an area enclosed by the curve C. By using Gauss' theorem to convert the area integrals to line integrals, we obtain

$$\oint_C H\mathbf{u}_0 \cdot \mathbf{n}ds = -\oint_C \mathbf{m} \cdot \mathbf{n}ds,$$

where $\mathbf{n}$ is the outward normal unit vector of C and ds the length element along the curve. If C coincides with a closed depth contour, the net geostrophic transport vanishes. Thus, we find that

$$\oint_{C(H)} \mathbf{m} \cdot \mathbf{n}ds = 0, \tag{14}$$

stating that the Ekman-layer transport across a closed depth contour must integrate to zero in a steady state (cf. Greenspan, 1968, Section 2.17). Accordingly, steady-state solutions to Eq. (13) exist only if Eq. (14) is fulfilled. In what follows we will focus on the along-isobath component of $\mathbf{u}_0$, which proves to be determined by this constraint.

In the inviscid limit (i.e. $\mathbf{m} = 0$), the relation (13) simply states that the barotropic component of the flow must be aligned with the depth contours:

$$\mathbf{u}_0 \cdot \nabla H = 0. \tag{15}$$

This is satisfied provided that the barotropic pressure p_0 is a function of the basin depth only, i.e. $p_0 = p_0(H)$ implying that

$$\nabla p_0 = \frac{dp_0}{dH}\nabla H.$$

By using this result, we can write the bottom velocity given by (12) as

$$\mathbf{u}_b = \left[\frac{g}{f}q_b(x, y) + \frac{1}{f\rho_r}\frac{dp_0}{dH}\right]\mathbf{k} \times \nabla H. \tag{16}$$

Evidently, the flow associated with $p_0(H)$ is aligned with the isobaths and its strength is proportional to the local bottom slope. In the inviscid limit, there is no further constraint on p_0; as long as it depends only on H it represents a steady-state solution, known as a geostrophic mode (Greenspan, 1968). It is important to recognize that if q_b varies along the isobaths, $p_0(H)$ cannot be chosen such that the bottom velocity vanishes everywhere. As a consequence, the variation of the flow along isobaths associated with a variation of q_b will always remain superimposed on the geostrophic mode. It is only in the special case when q_b is constant along the isobaths that Eq. (16) has a solution with zero bottom velocity. Thus, we make the important conclusion that variations in bottom buoyancy along the depth contours invariably result in along-isobath velocities at the bottom.

When the viscous boundary layers are thin compared to the depth scale of the bathymetry (see also Section 2e), the flow will still to the leading order be aligned with the depth contours, i.e. the leading-order bottom velocity is given by (16). However, the presence of friction brings the constraint (14) into play. To proceed with the analysis, we need to specify the properties of the boundary-layer transport $\mathbf{m}$. Employing Ekman theory (e.g. Pedlosky, 1987), we find that the boundary layer transports are related to the surface wind stress τ_w and the bottom stress τ_b according to

$$\mathbf{m} = -\mathbf{k} \times (\tau_w - \tau_b)/(\rho_r f). \tag{17}$$

For simplicity, we chose a linear representation of the bottom stress

$$\tau_b = \rho_r f h_e \mathbf{u}_b, \tag{18}$$

where h_e characterizes the depth of the bottom Ekman layer.

We now limit our attention to the case without wind forcing, i.e. $\tau_w = 0$; wind effects will be dealt with briefly in Section 2d. By using the explicit expression for the bottom boundary-layer transport in Eq. (14), we arrive at

$$\oint_{C(H)} \mathbf{u}_b \cdot d\mathbf{s} = 0, \tag{19}$$

where $d\mathbf{s}$ is the length element along the depth contour $C(H)$. It should be underlined that this relation does not imply that the bottom velocity is zero. Rather, by substituting the bottom-velocity given by (16) into Eq. (19), we obtain

$$\frac{g}{f} \oint_{C(H)} q_b(x, y) |\nabla H| ds + \frac{1}{f\rho_r} \frac{dp_0}{dH} \oint_{C(H)} |\nabla H| ds = 0.$$

This relation determines the pressure field $p_0(H)$ that yields zero net cross-isobath transport in the bottom Ekman layer. Straightforward rearrangements leads to

$$\frac{dp_0}{dH} = -g\rho_r \hat{q}(H), \tag{20}$$

where for notational convenience we have introduced the quantity

$$\hat{q}(H) = \oint_{C(H)} q_b |\nabla H| ds \left(\oint_{C(H)} |\nabla H| ds \right)^{-1}, \tag{21}$$

which is a slope-weighted measure of the mean-isobath buoyancy.

By using (20), we finally obtain the following expression for the bottom velocity

$$\mathbf{u}_b = \frac{g}{f} [\hat{q}(H) - q_b(x, y)] \nabla H \times \mathbf{k}. \tag{22}$$

We note that the bottom velocity is independent of the choice of reference density. Adding a constant to q does not alter the bottom velocity, although the magnitudes of $\hat{q}(H)$ and $q_b(x, y)$ will be altered. When the reference density ρ_r is chosen such that the densest water in the basin is characterized by $q = 0$, the flow component $\mathbf{u}_0$ is associated with cyclonic flow and comprises the entire bottom velocity in regions where the buoyancy anomaly vanishes.

It should be emphasized that the bottom velocity is independent of the actual strength of the bottom friction, though the effects of friction have been invoked to determine the free barotropic flow $\mathbf{u}_0$. The relation (21) specifies the barotropic flow when the bottom stress obeys the linear law given by Eq. (18). We note that the same result is also obtained when the bottom velocity is subjected to a no-slip boundary condition, provided that the viscosity is constant. We note furthermore that it is possible to extend the present analysis to encompass more general representations of the bottom stress. For the purpose of illustration, consider the quadratic bottom-stress law $\tau_b = \rho_r c_d |\mathbf{u}_b| \mathbf{u}_b$, where c_d is the drag coefficient. From Eq. (17) it follows that the net bottom boundary-layer transport across the closed depth contour $C(H)$ is given by

$$\oint_{C(H)} \mathbf{m} \cdot \mathbf{n} ds = \frac{c_d}{f} \oint_{C(H)} |\mathbf{u}_b| \mathbf{u}_b \cdot d\mathbf{s}.$$

By using the expression for the bottom velocity given by Eq. (22) and requiring that the net boundary-layer transport across the isobaths vanishes, we obtain the equation determining $\hat{q}(H)$ for the quadratic stress law:

$$0 = \frac{c_d g^2}{f^3} \oint_{C(H)} |\hat{q} - q_b| (\hat{q} - q_b) |\nabla H|^2 ds.$$

Generally, $\hat{q}(H)$ has to be calculated numerically from this expression. Also in this case, the calculated bottom velocity will be independent of the drag coefficient c_d and the viscosity.

c. Summary of the key results

The flow field is described by two components: $\mathbf{u} = \mathbf{u}_q + \mathbf{u}_0$. The first component is related to local buoyancy variations [see Eq. (10)] and given by

$$\mathbf{u}_q = \frac{g}{f}\mathbf{k} \times \int_{-H}^{z} \nabla_h q dz + \frac{g}{f} q_b \mathbf{k} \times \nabla H, \tag{23}$$

where the former term on the right-hand side is the thermal-wind velocity relative to the bottom and the latter term represents a depth-independent contribution to the along-isobath flow at the bottom. The second component $\mathbf{u}_0(H)$, which is purely barotropic, is present along the entire isobath; its strength is determined so that the net bottom Ekman transport across the closed isobath is zero. In the limit of small viscosity, the nonlocal flow component is given by

$$\mathbf{u}_0 = \frac{g}{f}\hat{q}(H)\nabla H \times \mathbf{k}. \tag{24}$$

In the special case where the bottom stress is proportional to the bottom velocity, the quantity $\hat{q}(H)$ is given by Eq. (21).

In Section 3, we will consider the depth-integrated flow. Straightforward calculations, using Eqs. (23, 24), show that the depth-integrated flow is described by $\psi = \psi_q + \psi_0$ where (see Walin *et al.,* 2004)

$$\psi_q(x, y) = -\frac{g}{f}\int_{-H}^{0} z \cdot q dz, \tag{25}$$

$$\psi_0(H) = -\frac{g}{f}\int_{0}^{H} \hat{q}(H) H dH. \tag{26}$$

d. A comment on wind forcing

The analysis can be extended to include wind stress acting on the surface. In this case, the constraint on the boundary-layer transport given by (14) yields

$$\oint_{C(H)} \tau_w \cdot d\mathbf{s} - \rho_* f h_e \oint_{C(H)} \mathbf{u}_b \cdot d\mathbf{s} = 0.$$

This relation states that the sum of the Ekman transports in the bottom and the surface layer must integrate to zero around a closed depth contour (Walin, 1972), or more generally around a closed H/f contour (Nøst and Isachsen, 2003). By using the expression for the bottom velocity given by (16), $p_0(H)$ can be determined. We find that the bottom velocity now is given by

$$\mathbf{u}_b = \left\{ \frac{g}{f} [\hat{q}(H) - q_b(x, y)] + \mathcal{V}_w(H) \right\} \nabla H \times \mathbf{k}, \tag{27}$$

where

$$\mathcal{V}_w(H) = \frac{1}{h_e f \rho_r} \oint_{C(H)} \boldsymbol{\tau}_w \cdot d\mathbf{s} \left(\oint_{C(H)} |\nabla H| ds \right)^{-1}. \tag{28}$$

We note that the wind stress induces a mean flow along the isobaths, which strength is inversely proportional to the Ekman depth. Thus, in contrast to the buoyancy-related flow, the strength of the wind-driven flow component depends on the magnitude of the bottom friction.

e. The cross-isobath circulation

In the preceding analysis, we have used the terms weak friction and small viscosity in a rather vague sense. For completeness, we provide a proper definition and take the opportunity to comment briefly on the cross-isobath circulation. Let us consider the case where the wind stress is zero, implying that the boundary-layer divergence is given by $-\nabla \cdot \mathbf{m} = h_e \nabla \times \mathbf{u}_b$, where h_e is the Ekman-layer depth. In this case Eq. (13) assumes the form

$$\mathbf{u}_0 \cdot \nabla H = h_e \nabla \times \mathbf{u}_b.$$

An elementary scale analysis of this equation shows that if the length-scale over which the flow varies normal to the isobaths is comparable to the length-scale of the bathymetry, then the ratio between the velocity components perpendicular and parallel to the isobaths is given by h_e/H. Note that this applies also in the presence of wind forcing provided that the mean wind stress acting along the isobath is comparable to the variation in wind stress over the same isobath (cf. Nøst and Isachsen, 2003). In the regime we consider, where h_e/H is taken to be small, the cross-isobath flow is thus determined by the vorticity of the leading-order bottom velocity, given by Eq. (22). It should be noted that the vertical velocity is exactly zero outside the bottom boundary layer, even at the order h_e/H (see Pedlosky, 1987, Section 4.9). Wind-induced Ekman pumping is required to create vertical motions in the interior of the fluid.

We note that the straightforward scaling considered above can break down on isobaths that pass through a saddle point. The reason is that Eq. (27) may predict different along-isobath velocities on depth contours that converge near the saddle point but enclose different sub-basins. If this occurs, the calculated along-isobath velocity becomes discontinuous at the saddle point, hereby violating the scaling assumption that the flow and the bathymetry varies over comparable length scales. This issue will not be considered further here, but we note that Welander (1968) discussed some qualitative aspects of a similar problem.

3. Illustrative examples

Based on the present theoretical results, we explore the steady-state circulation attained in a basin with a large-scale horizontal buoyancy difference and closed isobaths. We will provide three examples of this type of flow. To begin with, we investigate the flow in two cases where the buoyancy fields are described by simple analytical expression. Finally, we apply the present results in an attempt to deduce the velocity field from the buoyancy field obtained in a numerical simulation with an ocean-circulation model.

a. Flow in a bowl-shaped circular basin

We consider a bowl-shaped circular basin with the radius R, the coordinates r, θ, and the depth $H = H(r)$. Since the bottom slope is constant along the isobaths, $\hat{q}$ simply becomes the mean isobath buoyancy. Accordingly, Eq. (21) simplifies to

$$\hat{q}(H) = \frac{1}{L(H)} \oint_{C(H)} q_b ds, \tag{29}$$

where $L(H)$ is the length around the isobath H. For the purpose of obtaining a simple analytical solution, we chose a parabolic depth profile defined by

$$H(r) = H_M[1 - (r/R)^2], \tag{30}$$

and the buoyancy field

$$q = \frac{\Delta q}{2} [1 - (r/R) \sin(\theta)] \cdot \exp(z/d), \tag{31}$$

which ranges linearly from Δq in the "south" to zero in the "north" (note that $y = r \sin(\theta)$) and decreases exponentially with depth.

Making use of the Eqs. (24, 22), we find that the along-isobath velocity associated with p_0 is given by

$$v_0(r) = \frac{g\hat{q}(H)}{f} \left(- \frac{\partial H}{\partial r} \right), \tag{32}$$

and that the along-isobath velocity at the bottom is given by

$$v_b(r, \theta) = \frac{g}{f} [\hat{q}(H) - q_b(r, \theta)] \left(- \frac{\partial H}{\partial r} \right). \tag{33}$$

We note that the bottom velocity reverses sign where $q_b(r, \theta) = \hat{q}(H)$, i.e. where the local buoyancy equals the mean isobath buoyancy. In the present example, the bottom velocity is explicitly given by

$$v_b = \left(\frac{g \Delta q H_M}{fR} \right) r_*^2 \sin(\theta) \exp(-H_*),$$

where $r_* = r/R$ and $H_* = H(r)/d$. Note that v_b becomes exponentially small on isobaths located deeper than the scale depth d defined in Eq. (31). As illustrated in Figure 2d, the bottom current is cyclonic in the "northern" part of the basin and anticyclonic in the "southern" part.

Consider next the depth-integrated flow $\psi = \psi_q + \psi_0$, which can be calculated by using the general relations (25, 26) and the bathymetry and the buoyancy field specified by Eqs. (30, 31). After some calculations, we obtain

$$\psi_q = \frac{g\Delta q d^2}{f}\,[1 - r_* \sin(\theta)] \cdot [1 - (1 + H_*)\exp(-H_*)],$$

$$\psi_0 = -\frac{g\Delta q d^2}{f}\,[1 - (1 + H_*)\exp(-H_*)].$$

The structure of the depth-integrated flow depends on the ratio between the maximum basin depth H_M and the depth scale of the stratification d; quantities defined in Eqs. (30, 31). Figure 2 illustrates the case $d/H_M = 1/4$, implying that the stratification is shallow compared to the depth of the basin. In the absence of side boundaries, the buoyancy field described by (31) would be associated with a horizontally uniform thermal-wind velocity directed towards the east (i.e. flowing in the positive x-direction). However, the sloping side boundaries serve to redirect the circulation. The baroclinic flow component ψ_q, concentrated towards the southern part of the basin, forms an anticyclonic gyre that essentially recirculates the eastward thermal-wind transport in the interior of the basin. In the absence of a bottom Ekman layer, this would provide a steady-state circulation. However when friction is included, the flow ψ_0 must be added in order to cancel the net Ekman transport across the isobaths. The barotropic flow ψ_0 circulates cyclonically along the isobaths and is concentrated towards the rim of the basin, where the buoyancy varies on the depth contours. For the buoyancy field under consideration, the total stream function $\psi_q + \psi_0$ is comprised by two mirror-image gyres: one in the north spinning cyclonically and one in the south spinning anticyclonically.

It is of interest to examine the implied advection of buoyancy, which in a steady state must be balanced by some diabatic process. For the present buoyancy field, the thermal wind flow relative to the bottom is parallel to the isolines of buoyancy; cf. the Eqs. (23, 31). Accordingly, the buoyancy field is advected solely by the barotropic bottom velocity field, i.e. $\mathbf{u} \cdot \nabla q = \mathbf{u}_b \cdot \nabla q$. Making use of the Eq. (31) and the expression for v_b, one obtains

$$\mathbf{u}_b \cdot \nabla q = -\left(\frac{g\Delta q^2 H_M}{4fR^2}\right) r_*^2 \sin(2\theta)\exp(z/d - H_*).$$

(To visualize the horizontal structure of $\mathbf{u}_b \cdot \nabla q$, it is helpful to note that $r^2 \sin(2\theta) = 2xy$.) To balance this pattern of buoyancy advection, the water column must be subjected to cooling in the north-east quadrant and to heating in the north-west quadrant (the situation is reversed in the two southern quadrants). Note that the buoyancy advection

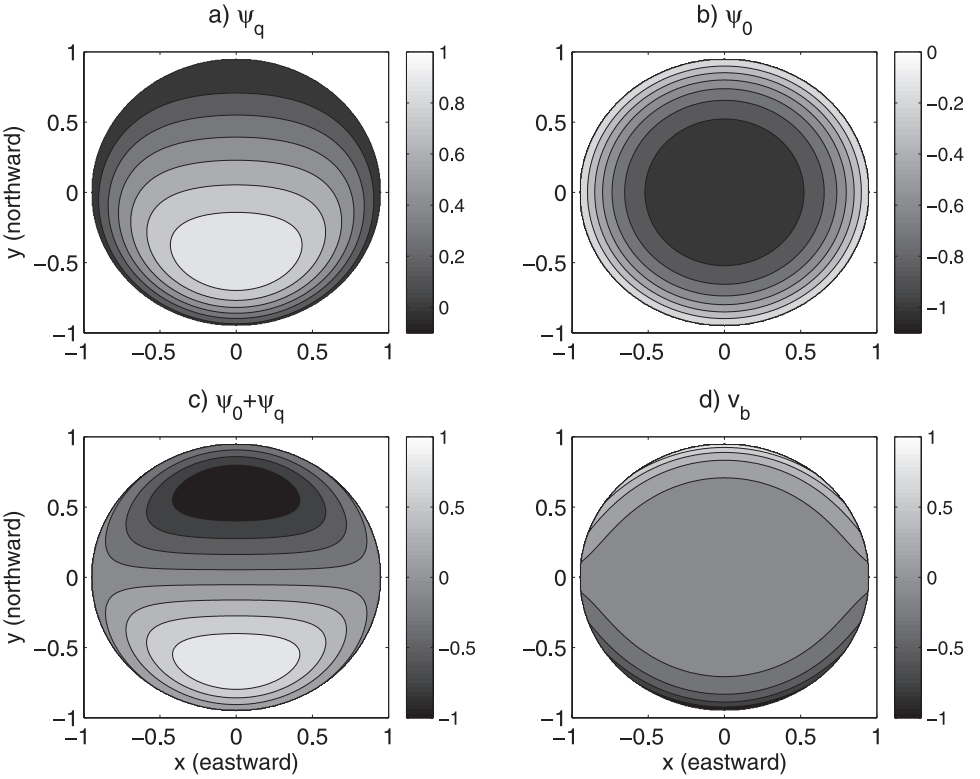

Figure 2. An analytical example of the flow in a circular parabolic basin where the buoyancy decreases with y; see Section 3a. Panels a–c show the depth-integrated flow associated with the baroclinic component ψ_q and the barotropic component ψ_0 as well as the total flow, given by $\psi_q + \psi_0$. Panel d shows the along-isobath bottom velocity, which in the present case reverses sign along $y = 0$. Note that the flow fields are presented on nondimensional form.

decreases exponentially with z as well as with basin depth. Further, since the bottom boundary-layer transport is directed 90 degrees to the left of the bottom current [see the Eqs. (17, 18)], the Ekman layer transports denser fluid down the slope in the north, while lighter fluid is transported up-slope in the south. Accordingly, the Ekman-layer flow acts to decrease the along-isobath variation of buoyancy and thereby also the bottom velocity; cf. Eq. (33).

b. A generalized two-layer flow

Consider the situation delineated in Figure 1, where a homogeneous surface layer with the depth $D(x, y)$ and the buoyancy anomaly Δq is encountered in a basin where the reminder of the water has a constant and slightly higher density (characterized by $q = 0$). Somewhere in the northern part of the basin, the denser water reaches the surface along a front. Thus, the central southern part of the basin is stratified in two layers. However on the

part of the slope covered by the buoyant water, where $D = H(x, y)$, as well as northward of the density front, a single vertically homogeneous layer is encountered.

To begin with, we focus on the local flow within the buoyant layer. By applying the Eqs. (23, 25), we obtain

$$\mathbf{u}_q = \frac{g\Delta q}{f}\,\mathbf{k} \times \nabla D,\ \psi_q(x, y) = \frac{g\Delta q D^2}{2f}.$$

We underline that these formula describe the flow in the entire buoyant layer: the results apply where the upper layer floats above the denser water as well as on the slope where the buoyant water reaches down to the bottom, implying that $D = H(x, y)$. Further, we note that the flow $\mathbf{u}_q$ is aligned with the contours of constant D. Accordingly this flow component does not cause any advection of depth of the buoyant layer, i.e. $\mathbf{u}_q \cdot \nabla D = 0$. Rather, $\mathbf{u}_q$ only recirculates the buoyant water. If D_M represents the maximum depth of the buoyant layer, the net recirculation (say M_q) is given by

$$M_q = \frac{g\Delta q {D_M}^2}{2f}. \tag{34}$$

Consider next the isobath-following barotropic flow, which must be present to cancel the cross-isobath Ekman transport induced by the local flow within the buoyant layer. To keep things simple, we assume that the bottom slope is constant along the isobaths, which allows us to use the formula (32) to calculate the barotropic flow associated with $p_0(H)$. On the depth contours that pass into the buoyant layer, we find that the barotropic along-isobath flow is given by

$$v_0(H) = \sigma\,\frac{g\Delta q}{f}\left(-\frac{\partial H}{\partial n}\right). \tag{35}$$

Here, n is a general coordinate (taken to increase towards the coast) perpendicular to the isobaths and σ is fraction of the depth contour covered by the buoyant water, i.e. $\sigma\Delta q$ is the mean isobath buoyancy, as defined by Eq. (29). We note that v_0 flows in a cyclonic sense and increases in strength with σ. Furthermore, v_0 comprises the entire velocity in the "north" and is zero on the isobaths situated below the buoyant layer. As evident from Figure 1, this barotropic flow acts to redistribute the pool of buoyant water. As a consequence, surface buoyancy fluxes and mixing must be present to keep the buoyancy field in a steady-state. Next, we focus on the bottom velocity within the buoyant layer. By using (33), we find that

$$v_b(H) = -(1 - \sigma)\,\frac{g\Delta q}{f}\left(-\frac{\partial H}{\partial n}\right), \tag{36}$$

showing that the bottom current is anticyclonic within the buoyant layer.

To estimate the volume transport associated with the nonlocal flow v_0, we assume that σ

is approximately constant on the isobaths traversing the buoyant layer (i.e. the length of the isobaths within the buoyant layer are assumed to be nearly equal). By integrating $v_0 \cdot H$ from the isobath $z = -D_M$ to the coast, we obtain

$$M_0 = \sigma \frac{g \Delta q D_M^2}{2f} = \sigma M_q. \tag{37}$$

This volume flow accounts for the diapycnal circulation, i.e. the advective buoyancy flux is given by $\Delta q \cdot M_0$. There are two things worth pointing out regarding M_0. To begin with, M_q always exceeds M_0, showing that a fraction $1 - \sigma$ of the buoyant water recirculates. Further, the strength of M_0 increases with the area of the slope covered by buoyant water (i.e. with σ). Thus, if the buoyant layer expands poleward, the strength of the nonlocal barotropic flow increases and accordingly also the diapycnal circulation. Conversely, a small pool of buoyant water in a basin occupied chiefly by dense water is associated with a weak diapycnal circulation. Presumably, these results can be used in the context of conceptual models of the thermohaline circulation (cf. Nilsson and Walin, 2001), an issue that we will return to in the discussion section.

Further, we note that the two-layer case can be related to the continuously stratified flow considered in Section 3a: The buoyancy distribution given by Eq. (31), with a constant north-south gradient, corresponds to a two-layer flow characterized by $\sigma = 1/2$, i.e. the strength of the depth-integrated northern cyclonic gyre equals that of the southern anticyclonic one. A continuous buoyancy distribution, for which the north-south gradient is more pronounced in the northern part of the basin, corresponds to a two-layer case having a value of σ closer to unity, implying that the northern gyre is stronger than the southern one.

c. A numerical simulation

We will now demonstrate that our theoretical considerations can be used to qualitatively reconstruct the velocity field in a numerical simulation from the modeled buoyancy field. We have used the MITgcm (Marshall *et al.,* 1997a,b) to conduct a simulation in a basin with sloping boundaries. The basin is rectangular, 6000×6000 km, and its depth increases linearly from the coast to a maximum depth of 3000 m, which is reached 2000 km from the coast. The central part of the basin has a flat bottom. (Note that the isobath structure is outlined by the stream function ψ_0 in Fig. 4b.)

The model uses Cartesian coordinates on an f-plane, with $f = 10^{-4}$ s^{-1}. The horizontal grid spacing is 100 km and the grid has 60×60 points. The model has 25 vertical levels with a spacing ranging from 50 m at the surface to 200 m at the bottom. Horizontal and vertical viscosities are 5000 m^2 s^{-1} and 10^{-3} m^2 s^{-1}, respectively, the vertical diffusivity is 10^{-4} m^2 s^{-1}. The horizontal mixing is represented by the GM scheme with the isopycnal diffusivity 10^3 m^2 s^{-1}. The density depends linearly on temperature; the thermal expansion coefficient is equal to $2 \cdot 10^{-4}$°C^{-1}. The boundary condition on the tangential velocity is no-slip on the solid boundaries. At the surface, the temperature is restored towards the

profile $\Delta T[\cos(\pi y/L) + 1]/2$, where $\Delta T = 20°\text{C}$ and L is the basin length. The restoring time scale is 12.5 days, implying that a deviation of one °C from the restoring temperature yields a surface heat flux of 185 W m^{-2}. (Note that the thermal restoring is so short that the sea surface temperature is essentially prescribed.) The model has been integrated for 2000 years, which allows the simulation to attain essentially a steady state.

Figure 3 shows the horizontal structure of the temperature and velocity at two different depths at the end of the simulation. At the surface the temperature is very close to the restoring temperature profile. However at 600 m, in the lower part of the thermocline, the warmest water is encountered in the central basin. The bottom velocity (illustrated by the arrows closest to the boundaries in Fig. 3) is cyclonic in the northwestern part of the basin, while it is anticyclonic in the southeastern part. Note that the bottom temperatures at the two locations where the bottom current reverses direction are approximately equal. This is in agreement with the results presented in Section 2, cf. Eq. (33). It should be underlined that the temperature field is not prescribed in the model. At the end of the simulation, a dominant balance between horizontal advection and vertical diffusion is established in interior of the model domain. Note furthermore that the Rossby number in the simulation is on the order of 10^{-2}, implying that the vertical motions are weak and primarily occur within the bottom Ekman layer on the slope; see Spall (2004) for a further discussion of the vertical circulation in an f-plane basin with sloping side boundaries.

We now take the simulated temperature field and use the results of Section 2 in an attempt to reconstruct the modeled velocity field. A difficulty in comparing the theory with the model results is that the bottom Ekman layer extends over one or two grid cells in the simulation. Thus, the "top" of the boundary layer may be encountered relatively far above the bottom in the simulation. As a consequence, it is not straightforward to compare the bottom velocities quantitatively. Instead we focus on the depth-integrated flow, anticipating that the theoretical results are capable of describing the qualitative features of this flow field. For this purpose, we have used the same procedure as in the two analytical examples considered above: To calculate the flow, we have employed Eqs. (25, 26) and the definition (21) on the simulated temperature field; Figure 4 shows the results. As in the previous analytical examples, the baroclinic flow ψ_q essentially recirculates the buoyant water masses. We note that the theoretically calculated total flow $\psi_q + \psi_0$ is in qualitative agreement with the depth-integrated flow diagnosed directly for the simulated velocity field. (The fact that the theoretical flow has a slightly larger amplitude is presumably due to a poor resolution of the Ekman layer and the presence of lateral viscosity in the simulation.) Based on Eq. (37), we can estimate the degree of recirculation (i.e. the parameter σ) in the numerical model: The ratio between ψ_0 and ψ_q is about 1/2, suggesting that some 50% of the depth-integrated flow recirculates within the pool of buoyant water visible in Figure 3.

It should be noted that although the agreement between the model results and the theory are reasonable, the coarse vertical resolution in the model precludes a more rigorous quantitative comparison. In fact, the present numerical calculation cannot unambiguously

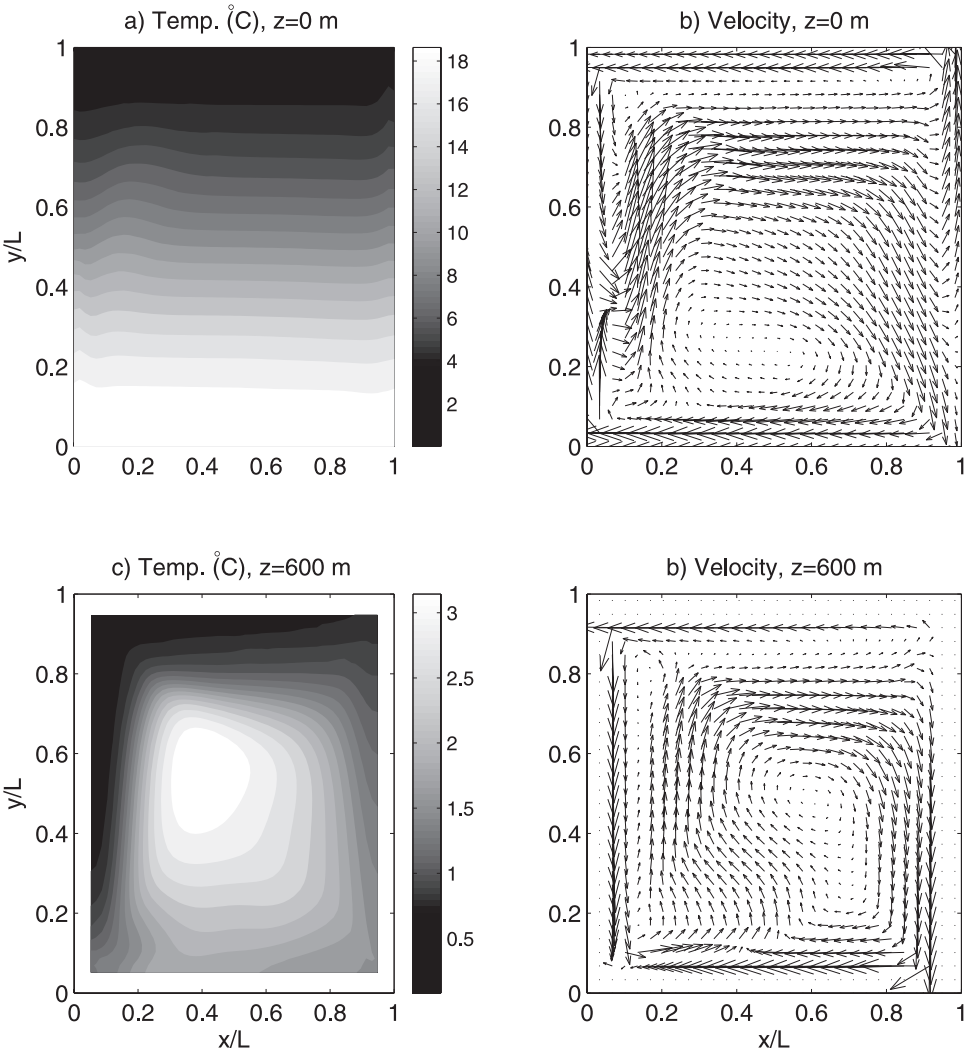

Figure 3. The steady-state temperature and horizontal velocity structure from a numerical *f*-plane simulation conducted in a basin with sloping side boundaries (see Section 3c). The maximum horizontal velocity in the simulation is on the order of 0.1 m s^{-1}. Note that in the model, the rate of change of temperature is affected by advection, vertical and horizontal diffusion, and parameterized convection.

demonstrate the controlling influence of the vertical viscosity in the Ekman layer since the model has other forms of dissipation (including some numerical diffusion) that may serve the same role. However, this is a numerical problem rather than a limitation of the theory, which applies for nearly-inviscid flows with a low Rossby number.

It is interesting to note that the present numerically calculated flow has qualitative

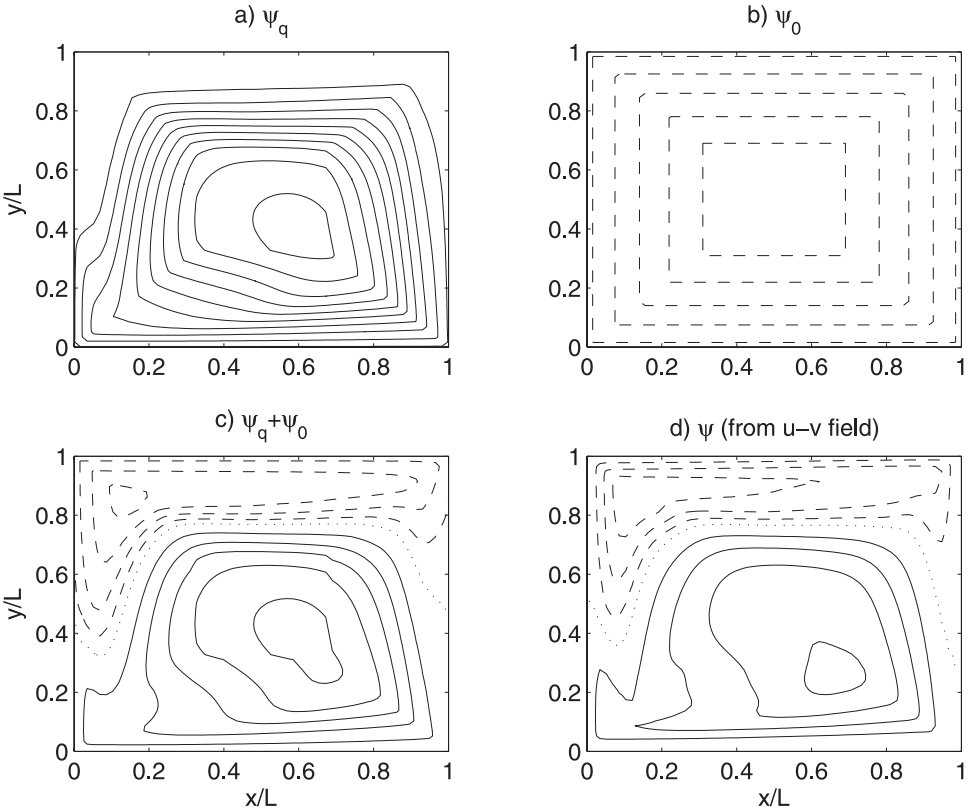

Figure 4. Horizontal transport stream functions pertaining to the numerical *f*-plane simulation. The contour interval is 5 Sv (in c and d are also the contours −2.5 and −7.5 Sv drawn) and negative contours are dashed and the zero contour is dotted. Panels a–c show the flow calculated from the simulated temperature field employing Eqs. (25, 26). Panel d shows the total stream function calculated from the simulated velocity field.

similarities with the numerical results obtained by Spall (2005) using a rectangular basin with open isobaths. In his model, the isobaths are blocked by a vertical wall at the southern (i.e. warm) end of the basin. Away from the southern wall, where the depth gradually increases from the coastal boundary, the bottom flow tends to be cyclonic and aligned with the isobaths. Furthermore, the strength of the cyclonic bottom flow tends to increase with decreasing bottom buoyancy, a state of affairs consonant with the present theoretical considerations. We note that Spall provides a somewhat different interpretation of the intensification of the cyclonic bottom flow in the northern part of the basin.

Finally, it is relevant to mention that preliminary results suggest that the present theoretical considerations also are capable of qualitative reproducing the time-mean velocity field in the eddy-permitting *f*-plane simulations reported by Walin *et al.* (2004). This indicates that even in the presence of time-dependent eddies, the time-mean bottom

velocity evolves toward the state in which the cross-isobath Ekman transport integrates to zero on closed depth contours. However, a further analysis of the numerical simulations reported by Walin *et al.* is outside the scope of the present study.

4. Discussion

We have theoretically investigated steady-state flows in bowl-shaped basins on an f-plane in the presence of weak bottom friction. We have shown that the free along-isobath barotropic flow (i.e. the geostrophic mode) can be determined by requiring that the net cross-isobath Ekman transport vanishes in a steady state. This constraint permits the specification of the geostrophic velocity field on closed isobaths from a knowledge of the buoyancy distribution. An important result is that the bottom velocity is determined by the buoyancy distribution around the entire closed depth contour. As a consequence, the steady-state circulation in a bowl-shaped basin is nonlocal in nature. The transient dynamics have not been considered in the present work. We note, however, that the barotropic pressure p_0 spins up on the time-scale $f^{-1}(H/h_e)$—typically on the order of weeks to months—provided that the basin is small compared to the barotropic Rossby radius (cf. Walin, 1972; Cederlöf, 1988; Hallberg and Rhines, 1996; Isachsen *et al.,* 2003). Accordingly, the present steady-state results should describe the response of the isobath-following barotropic flow to changes in bottom buoyancy that occur on seasonal (or longer) time scales.

Emphasis has been given to the geophysically interesting case where the surface buoyancy decreases northwards in a basin with closed isobaths. The theoretically deduced circulations as well as the numerically simulated flow have the following general characteristics:

1. The bottom velocity is aligned with the depth contours and flows cyclonically (anticyclonically) where the buoyancy is less (larger) than the mean buoyancy on the isobath.
2. The vertical extent of the flow is set by the depth of the stratification, i.e. the bottom velocity is zero on depth contours where the buoyancy is constant.
3. The depth-integrated flow forms two gyres; a cyclonic gyre harboring denser water and an anticyclonic one harboring lighter water.
4. The northward flow along the western margin separates from the coast at the gyre boundary.

It deserves to be noted that the present f-plane circulations, in a broad sense, reproduce some elements of the circulation in the northern North Atlantic. A particularly intriguing feature of the analysis is that a "subpolar gyre" and cyclonic boundary-trapped currents emerge in the "northern" part of the basin, even in the absence cyclonic wind forcing.

It should be emphasized that the beta effect introduces new physics. We note, however,

that some features characterizing the present *f*-plane circulations are encountered also in numerical simulations conducted in bowl-shaped single-hemisphere basins in the absence of wind forcing (see Winton, 1997; Spall and Pickart, 2001; Park and Bryan, 2001). These simulations, which are driven by an imposed surface buoyancy gradient and the presence of vertical diffusivity, yield depth-integrated flows comprised by two gyres. In the simulations, cyclonic circulation is consistently encountered in the northern part of the basin—a feature that tend to be absent in simulations conducted in basins with a flat bottom (Winton, 1997; Park and Bryan, 2001).

In the analysis of the two-layer flow in Section 3b, we found that the nonlocal barotropic flow was proportional to the recirculating baroclinic flow; see Eq. (37). Furthermore we noted that the barotropic flow $\mathbf{u}_0$, which arises due to the presence of bottom friction, alone accounts for the buoyancy advection. These findings are interesting in the context of the classical thermocline scaling, which essentially concerns the volume balance of the pool of buoyant thermocline water (cf. Welander, 1986). Two competing processes are assumed to affect the pool of buoyant water: A gain due to vertical mixing and a loss due to poleward advection. The strength of the latter process is estimated from the thermal-wind relation employing the equator-to-pole buoyancy difference. A conceptual difficulty, however, is that the thermal-wind relation actually ties the north–south buoyancy difference to the strength of the east–west flow, rather than to the strength of the poleward flow. Accordingly, the thermocline scaling presumes that the meridional transport of buoyant water is proportional to the zonal one—a state of affairs in broad agreement with results from idealized numerical simulations (cf. Park and Bryan, 2000; Nilsson *et al.,* 2003). To examine the underlying physics, Marotzke (1997) conducted a theoretical analysis of the circulation in a flat-bottomed one-hemisphere basin where vertical mixing was assumed to occur only near the side boundaries. His analysis predicted that the east–west and the north–south buoyancy differences are coupled. Evidently, this also couples the transports. The present *f*-plane analysis also predicts that the zonal thermal-wind transport is proportional to the poleward transport of buoyant water. However in the present case, it is the effect of bottom friction that connects the transports, rather than the fact that the zonal buoyancy difference mirrors the meridional one.

In this context, it should be noted that a sloping bottom boundary may become "slippery" in a stratified fluid (cf. Garrett *et al.,* 1993; MacCready and Rhines, 1993; Chapman and Lentz, 1994). In essence, what happens is that the cross-isobath flow within the bottom Ekman layer acts to modify the near-bottom buoyancy field in such a way that the associated geostrophic shear reduces the velocity at the bottom. If unopposed, this processes will eliminate the buoyancy anomaly at the bottom and thereby also the bottom velocity and the associated bottom stress. As a consequence mixing must be present in order to maintain the along-isobath variation of the bottom buoyancy and the associated bottom velocity; see Eq. (22). Furthermore, the analytical examples considered in Section 3 suggest that, outside the Ekman layer, the buoyancy field is primarily advected by the barotropic velocity, i.e. the buoyant water in the upper ocean will essentially recirculate in

the absence of the barotropic flow. Thus, to obtain a diapycnal circulation (i.e. a thermohaline circulation) in a bowl-shaped basin requires mixing, which creates bottom buoyancy anomalies, and bottom friction, which creates the barotropic along-isobath flow that advects the buoyancy field.

Finally we speculate on whether topography can have a stabilizing influence on a thermohaline ocean circulation. To be concrete, we imagine an increased freshwater input to the Nordic Seas, serving to decrease the density difference between the water masses in the central basin and the inflowing warm Atlantic water. The generally anticipated response is a reduced exchange across the Greenland–Scotland Ridge, which would further accelerate the freshening and potentially destabilize the system (see e.g. Hansen *et al.,* 2004). This scenario presumes that the cross-ridge flow is essentially controlled by the local buoyancy contrast.

The present theoretical and numerical results, however, suggest that the circulation in general also has a barotropic component, which traces the isobaths. The strength of this barotropic flow reflects the buoyancy difference over the entire stretch of the closed isobaths, see Eq. (22). Thus, a local buoyancy anomaly in "high latitudes" should only have a weak effect on the barotropic flow. Furthermore, the buoyancy anomaly must penetrate down to the isobaths that guide the barotropic flow to make an impact. Accordingly, the barotropic flow should be essentially insensitive to shallow surface-trapped freshwater anomalies. It should be noted that the strength of the barotropic current decreases if the large-scale buoyancy contrast is diminished. As a consequence, the presence of a non-locally controlled barotropic flow does not necessarily remove Stommel's positive feedback between salinity- and flow-anomalies (cf. Nilsson and Walin, 2001). However, the strength of this potentially destabilizing feedback is presumably reduced in basins with closed isobaths.

We emphasize that the present results, pertaining to flow along closed isobaths on an f-plane, may not be directly applicable for barotropic flows on essentially open H/f-contours in the northern North Atlantic. We note, however, that the northward flow of Atlantic water off the Norwegian coast has one nearly barotropic branch, confined on the isobaths that extends southward over the Greenland–Scotland Ridge (e.g. Orvik *et al.,* 2001). This current, known as the Norwegian Atlantic Slope Current, carries roughly half of the Atlantic water flowing northwards through the Nordic Seas. From the perspective of the present study and the results reported by Walin *et al.* (2004), the barotropic slope current appears to be central for the thermohaline exchange over the ridge—a process traditionally viewed as a primarily baroclinic phenomenon. An intriguing question is whether the strength of Norwegian Atlantic Slope Current is affected by the bottom buoyancy distribution in North Atlantic. However, further investigations on the dynamics of non-locally controlled barotropic flows are required to answer this question.

Acknowledgments. This work was supported by the Swedish Science Research Council and the Swedish National Space Board. We thank M. Spall and an anonymous referee for providing constructive reviews of our original manuscript. Discussions with J. LaCasce and O. A. Nøst are also

acknowledged. Further, we thank the Knut and Alice Wallenberg Foundation for funding the Linux Cluster "Otto" and the staff at the National Center for Super Computing in Linköping for their assistance.

REFERENCES

Bogden, P. S., R. E. Davis and R. Salmon. 1993. The North Atlantic circulation: Combining simplified dynamics with hydrographic data. J. Mar. Res., *51,* 1–52.

Cederlöf, U. 1988. Free-surface effects on spin-up. J. Fluid Mech., *187,* 395–407.

Chapman, D. C. and S. J. Lentz. 1994. Trapping of a coastal density front by the bottom boundary layer. J. Phys. Oceanogr., *24,* 1464–1479.

Garrett, C., P. MacCready and P. Rhines. 1993. Boundary mixing and arrested Ekman layers: rotating stratified flow near a sloping boundary. Annu. Rev. Fluid Mech., *25,* 291–323.

Greenspan, H. P. 1968. The Theory of Rotating Fluids, Cambridge University Press, first edition, 328 pp.

Hallberg, R. and P. Rhines. 1996. Buoyancy-driven circulation in an ocean basin with isopycnals intersecting the sloping boundary. J. Phys. Oceanogr., *26,* 913–940.

Hansen, B., S. Østerhus, D. Quadfasel and W. Turrell. 2004. Already the day after tomorrow? Science, *305,* 953–954.

Isachsen, P. E., J. H. LaCasce, C. Mauritzen and S. Häkkinen. 2003. Wind-driven variability of the large-scale recirculation flow in the Nordic Seas and the Arctic Ocean. J. Phys. Oceanogr., *33,* 2434–2550.

Kamenkovich, V. M. 1963. On the theory of the Antarctic Circumpolar Current. Tr. Inst. Okeanol., *56,* 245–306.

Lentz, S. J. and K. R. Helfrich. 2002. Buoyant gravity currents along a sloping bottom in a rotating fluid. J. Fluid Mech., *464,* 251–278.

MacCready, P. and P. B. Rhines. 1993. Slippery bottom boundary layers on a slope. J. Phys. Oceanogr., *23,* 5–22.

Marotzke, J. 1997. Boundary mixing and the dynamics of three-dimensional thermohaline circulations. J. Phys. Oceanogr., *27,* 1713–1728.

Marshall, D. 1995. Influence of topography on the large-scale ocean circulation. J. Phys. Oceanogr., *25,* 1622–1635.

Marshall, J., A. Adcroft, C. Hill, L. Perleman and C. Heisey. 1997a. A finite-volume, incompressible Navier Stokes model for studies of the ocean on parallel computers. J. Geophys. Res., *102 (C3),* 5753–5766.

Marshall, J., C. Hill, L. Perleman and A. Adcroft. 1997b. Hydrostatic, quasi-hydrostatic, and non-hydrostatic ocean modeling. J. Geophys. Res., *102 (C3),* 5733–5752.

Nilsson, J., G. Broström and G. Walin. 2003. The thermohaline circulation and vertical mixing: does weaker density stratification give stronger overturning? J. Phys. Oceanogr., *33,* 2781–2795.

Nilsson, J. and G. Walin. 2001. Freshwater forcing as a booster of thermohaline circulation. Tellus, *53A,* 629–641.

Nøst, O. A. and P. E. Isachsen. 2003. The large-scale time-mean ocean circulation in the Nordic Seas and the Arctic Ocean estimated from simplified dynamics. J. Mar. Res., *61,* 175–210.

Orvik, K. A., Ø. Skagseth and M. Mork. 2001. Atlantic inflow to the Nordic Seas: current structure and volume fluxes from moored current meters, VM-ADCP and SeaSoar-CTD observations, 1995–1999. Deep-Sea Res., *48,* 937–957.

Park, Y.-G. and K. Bryan. 2000. Comparison of thermally driven circulation from a depth-coordinate model and an isopycnal model. Part I: scaling-law sensitivity to vertical diffusivity. J. Phys. Oceanogr., *30,* 590–605.

—— 2001. Comparison of thermally driven circulation from a depth-coordinate model and an

isopycnal model. Part II: the difference and the structure of the circulation. J. Phys. Oceanogr., *31,* 2612–2624.

Park, Y.-H. and J. M. Guernier. 2001. A simple method for diagnosing the bottom current field of the World's Oceans. J. Phys. Oceanogr., *31,* 972–991.

Pedlosky, J. 1987. Geophysical Fluid Dynamics, Springer-Verlag, 2nd ed., 710 pp.

Spall, M. A. 2004. Boundary currents and water mass transformation in marginal seas. J. Phys. Oceanogr., *34,* 1197–1213.

—— 2005. Buoyancy-forced circulations in shallow marginal seas. J. Mar. Res., *63,* 729–752.

Spall, M. A. and R. S. Pickart. 2001. Where does dense water sink? a subpolar gyre example. J. Phys. Oceanogr., *31,* 810–826.

Walin, G. 1972. On the hydrographic response to transient meteorological disturbances. Tellus, *24,* 169–186.

Walin, G., G. Broström, J. Nilsson and O. Dahl. 2004. Baroclinic boundary currents with downstream decreasing buoyancy; a study of an idealized Nordic Sea system. J. Mar. Res., *62,* 517–543.

Welander, P. 1959. An advective model of the ocean thermocline. Tellus, *11,* 309–318.

—— 1968. Wind-driven circulation in one- and two-layer oceans of variable depth. Tellus, *20,* 1–16.

—— 1986. Thermohaline effects in the ocean circulation and related simple models, *in* Large-Scale Transport Processes in the Oceans and Atmosphere, J. Willebrand and D. L. T. Anderson, eds., D. Reidel Publishing, 163–200.

Winton, M. 1997. The damping effect of bottom topography on internal decadal-scale oscillations of the thermohaline circulation. J. Phys. Oceanogr., *27,* 203–307.

Received: *23 September, 2004;* revised: *1 February, 2005.*